
Article:
Arran, C., Holec, M., Sherlock, M. et al. (2025) The accuracy of multi-group models for nonlocal electron transport in magnetized plasmas. Physics of Plasmas. 043908. ISSN: 1089-7674

https://doi.org/10.1063/5.0250147

RESEARCH ARTICLE | APRIL 30 2025

The accuracy of multi-group models for nonlocal electron transport in magnetized plasmas

C. Arran ; M. Holec ; M. Sherlock ; M. Marinak ; C. P. Ridgers

Phys. Plasmas 32, 043908 (2025)
https://doi.org/10.1063/5.0250147
CHORUS

The accuracy of multi-group models for nonlocal electron transport in magnetized plasmas

Cite as: Phys. Plasmas **32**, 043908 (2025); doi: 10.1063/5.0250147
Submitted: 22 November 2024 · Accepted: 20 February 2025 ·
Published Online: 30 April 2025

C. Arran,[1,2,a] M. Holec,[2,b] M. Sherlock,[2] M. Marinak,[2] and C. P. Ridgers[1,c]

AFFILIATIONS

[1]York Plasma Institute, University of York, Heslington, York YO10 5DD, United Kingdom
[2]LLNL, 7000 East Ave., Livermore, California 94550, USA

[a]**Present address:** Cockcroft Institute, Physics Department, Lancaster University, Bailrigg, Lancaster LA1 4YW, United Kingdom.
[b]**Present address:** Xcimer Energy Corporation, Denver, Colorado 80238, USA.
[c]**Author to whom correspondence should be addressed:** christopher.ridgers@york.ac.uk

ABSTRACT

In the extreme conditions of inertial confinement fusion experiments, heat flow plays a vital role, but local diffusive models frequently break down and overestimate the heat flow. The situation becomes more complicated again in the significant magnetic fields generated during laser–plasma interactions or in magnetized fusion schemes. Accurate non-local and magnetized heat flow computations can be carried out using Vlasov–Fokker–Planck (VFP) simulations, but these are computationally expensive. There is, therefore, significant interest in using faster multi-group models to accurately calculate the non-local heat flow in magnetized plasmas. We benchmark two such multi-group models for calculating the heat flow, M1 and `hybrid-AWBS-BGK`, against diffusive models and full VFP simulations, before applying the models to realistic example test cases, both magnetized and unmagnetized. We find that the multi-group models generally perform very well for moderate non-localities up to $k\lambda_{\mathrm{mfp}} \sim 0.01$, but the computational cost increases dramatically. `hybrid-AWBS-BGK` performs more effectively than M1 at high non-localities, up to $k\lambda_{\mathrm{mfp}} \sim 1$, due to its adaptive solver and robust P1 closure, but tends to fail in very strong magnetic fields. Both codes are much faster than VFP simulations but are still slow in steep temperature gradients.

I. INTRODUCTION

Understanding heat flow is critical to modeling high temperature plasma interactions, in particular, inertial confinement fusion. Here, steep temperature gradients drive strong heat flows and create strongly anisotropic and non-Maxwellian plasmas. As heat flow is primarily carried by high energy electrons, with long mean free paths, even small changes to the high velocity part of the electron distribution can greatly change the nature of the heat flow. For sufficiently steep temperature gradients or long mean free paths, the fluid models of plasmas break down and heat flow can no longer be described by diffusive models. Instead, electrons can travel several temperature scale lengths in the plasma before colliding, making heat flow nonlocal.[1,2]

This nonlocal transport has complex consequences for ICF. On one hand, it has been suggested that this nonlocal transport may mitigate instability growth.[3,4] On the other hand, it may increase the degree of pre-heat in the capsule and reduce the final compression.[5] The effects of nonlocal transport are particularly important in the steep temperature gradients at the hohlraum wall and during burn wave propagation, with simulations showing Knudsen numbers $\lambda_{\mathrm{mfp}}/L \sim 0.01 - 1$.[6–8] The principal method of modeling ICF plasmas with flux-limited fluid codes often fails to match experimental results in these extremely steep temperature gradients.

Modeling these dynamics is especially difficult when plasmas are magnetized. Magnetic fields change both the magnitude and direction of the heat flow[9,10] and experiments have found that strong magnetic fields can localize transport, making diffusive models more accurate than first expected.[11,12] Simulations of ICF experiments have demonstrated that strong magnetic fields are generated in the laser–plasma interaction, which have the ability to inhibit thermal transport and raise plasma temperatures.[13–15] Promisingly, improved performance using an externally imposed field has been demonstrated in both direct-drive ICF[16,17] and indirect-drive ICF,[18,19] fueling research into magnetized liner inertial fusion.[20,21] This makes understanding heat flow and the role of nonlocal transport in magnetic fields increasingly important.

In order to accurately capture nonlocal electron thermal transport, one must solve for the electron distribution function, including the high energy and lower collisionality electrons responsible for the thermal transport. An *ab initio* treatment involves the direct solution of the Vlasov–Fokker–Planck equation for the electron distribution function. The Vlasov–Fokker–Planck (VFP) codes `IMPACT` and K2 were developed to simulate precisely the interplay of nonlocal electron transport and magnetic fields.[22,23] VFP codes are currently too computationally expensive and not robust enough to couple to integrated design radiation-hydrodynamics codes, such as HYDRA. Several reduced multi-group models have been developed, which break the heat flow down into contributions from electrons of different energies, less accurate than a full solution of the VFP equation but considerably faster. The Schurtz–Nicolai–Busquet (SNB) model[24] has been included in HYDRA and shown to accurately simulate nonlocal transport in the absence of magnetic fields over a wide range of parameters.[25] Models including magnetic fields have also been developed, but these have yet to be benchmarked against VFP.

In this paper, we will present benchmarking of nonlocal transport models including magnetic fields against the VFP codes `IMPACT` and K2. We focus on comparing the M1 model, which uses an entropic closure,[26,27] and the `hybrid-AWBS-BGK` code developed from Ref. 28, which uses a simpler closure and collision operator but a more advanced adaptive solver. In Sec. II, we will describe these codes and models. In Sec. III, we demonstrate that the models agree as expected when the transport is local and in Sec. IV we compare the model predictions in the more interesting nonlocal case. Finally, in Sec. V, we look at more complex problems relevant to indirect drive ICF hohlraums.

II. DIFFERENT MODELS

A. Equations for moments of the distribution function

All of the models considered here describe the evolution of electrons under the influence of the Lorentz force and collisions by solving the Vlasov–Fokker–Planck equation for the electron distribution function

$$\frac{\partial f_e}{\partial t} + \underline{v}\cdot\underline{\nabla} f_e - e(\underline{E} + \underline{v}\times\underline{B})\cdot\underline{\nabla}_v f_e = \left(\frac{\partial f_e}{\partial t}\right)_{\text{coll}}. \tag{1}$$

In order to reduce the dimensionality of this problem and make the problem more tractable, we consider the electron distribution function as a sum of three angular moments, taken as integrals over the solid angle Ω,

$$f_0(v) \equiv \int\int f_e(\underline{v})\,\mathrm{d}^2\Omega, \tag{2}$$

$$\underline{f_1}(v) \equiv \int\int f_e(\underline{v})\hat{\underline{v}}\,\mathrm{d}^2\Omega, \tag{3}$$

$$\underline{\underline{f_2}}(v) \equiv \int\int f_e(\underline{v})\hat{\underline{v}}\otimes\hat{\underline{v}}\,\mathrm{d}^2\Omega,, \tag{4}$$

where $\hat{\underline{v}}$ is the unit vector.

The heat flow due to electron transport can then be calculated from the first moment of the distribution function as

$$\underline{q} = \int\int\int f_e \frac{1}{2} m_e v^2 \underline{v}\, v^2 \mathrm{d}^2\Omega \mathrm{d}v = \frac{m_e}{2}\int \underline{f_1} v^5 \mathrm{d}v. \tag{5}$$

We also make two physical approximations. First, we assume that the distribution function is slowly varying compared to the collision timescale, such that $\partial_t f_e \ll (\partial_t f_e)_{\text{coll}}$, allowing us to neglect $\partial_t f_e$; we shall see later that this assumption breaks down for strong transport. This essentially removes any history from the dynamics and allows us to solve the distribution function in a quasi-static situation, where electrons have enough time to move around such that we can find moments of the distribution function f_0, $\underline{f_1}$, and $\underline{\underline{f_2}}$ which are all consistent with one another.

Second, we use an AWBS form for the collision operator,[29] which considers superthermal electrons colliding with a thermal background of electrons and ions. We assume that the distribution function is not very far from an isotropic Maxwellian distribution given by

$$f_0^m = 4\pi f_e^m = \frac{4\pi n_e}{\left(2\pi v_{\text{th}}^2\right)^{\frac{3}{2}}}\exp\left(-\frac{v^2}{2v_{\text{th}}^2}\right), \tag{6}$$

where the thermal velocity is given by $v_{\text{th}} = \sqrt{eT_e/m_e}$ for a temperature in electronvolts. We further assume that the distribution function relaxes toward this Maxwellian through friction at a rate given by the electron–electron collision frequency ν_{ee}, neglecting the effect of velocity diffusion. Finally, we assume that ion collisions only enter through angular diffusion, modeling collisions of mobile electrons with stationary ions. This gives

$$\left(\frac{\partial f_e}{\partial t}\right)_{\text{coll}} = \nu_{ee} v \frac{\partial}{\partial v}\left(f_e - f_e^m\right) + \frac{\nu_{ee}+\nu_{ei}}{2}\frac{\partial^2}{\partial\Omega^2} f_e, \tag{7}$$

where we use Spitzer's 90° scattering rates[30] $\nu_{ee} = \frac{4\pi}{m_e^2}\left(\frac{e^2}{4\pi\varepsilon_0}\right)^2 n_e \times \ln\Lambda_{ee} v^{-3}$ and $\nu_{ei} = \frac{4\pi}{m_e^2}\left(\frac{e^2}{4\pi\varepsilon_0}\right)^2 Z n_e \ln\Lambda_{ei} v^{-3}$.

In total, these assumptions lead to two equations for the moments of the distribution function given by

$$v\underline{\nabla}\cdot\underline{f_1} - \frac{e}{m_e v^2}\frac{\partial}{\partial v}\left(v^2\underline{f_1}\cdot\underline{E}\right) = \nu_{ee} v\frac{\partial}{\partial v}\left(f_0 - f_0^m\right), \tag{8}$$

$$v\underline{\nabla}\cdot\underline{\underline{f_2}} - \frac{e}{m_e v^2}\frac{\partial}{\partial v}\left(v^2\underline{\underline{f_2}}\cdot\underline{E}\right) - \frac{e}{m_e v}\underline{\underline{f_2}}\cdot\underline{E} + \frac{e}{m_e v} f_0\underline{E} + \frac{e}{m_e}\underline{f_1}\times\underline{B} = \nu_{ee} v\frac{\partial}{\partial v}\underline{f_1} - (\nu_{ee}+\nu_{ei})\underline{f_1}. \tag{9}$$

With these coupled differential equations for f_0 and $\underline{f_1}$, the next step is therefore to determine a form for $\underline{\underline{f_2}}$.

B. M1 model

1. Entropic closure

Crucially, the M1 model includes the effect of the second-order anisotropy using $\underline{\underline{f_2}}$ but closes the angular hierarchy here, such that $\underline{\underline{f_2}}$ is purely a function of f_0 and $\underline{f_1}$. The simplest possible closure here, with isotropic $\underline{\underline{f_2}} = f_0\underline{\underline{I}}/3$, is called the P1 closure.

The M1 closure, on the other hand, is designed to maximize the entropy given by $\int\int\int(f_e\ln f_e - f_e)v^2\,\mathrm{d}^2\Omega\,\mathrm{d}v$, subject to satisfying the moment Eqs. (2)–(4). This entropy is maximized when $\underline{\underline{f_2}}$ is given by

$$\underline{\underline{f_2}} = \left[\frac{1}{3}\underline{\underline{I}} + \frac{1}{2}\frac{f_1^2}{f_0^2}\left(1+\frac{f_1^2}{f_0^2}\right)\left(\frac{\underline{f_1}\otimes\underline{f_1}}{f_1^2} - \frac{1}{3}\underline{\underline{I}}\right)\right] f_0 \equiv \underline{\underline{\chi}} f_0. \tag{10}$$

This permits a second-order anisotropy described by $\underline{\underline{\chi}}$, with the degree of the anisotropy given by $0 \le f_1^2/f_0^2 \le 1$. At the lower limit, this reproduces the P1 closure. If the anisotropy reaches the upper limit, however, $\underline{\underline{f_2}}$ becomes entirely directed along the anisotropy and zero elsewhere, with $\underline{\underline{f_2}} = (\hat{\underline{f_1}} \otimes \hat{\underline{f_1}}) f_0$. If $|f_1| > f_0$ at any point, the system breaks down, with the electron distribution function becoming negative.

2. Solving the M1 model

With the M1 closure, we have three equations relating f_0, $\underline{f_1}$, and $\underline{\underline{f_2}}$. For convenience, we switch to using energy as the variable of interest as $\varepsilon = m_e v^2/2$ and replace the collision frequency with a stopping force $S_\varepsilon = m_e v \nu_{ee}$. We keep the Coulomb logarithm constant with velocity, such that $S_\varepsilon \propto \varepsilon^{-1}$. We then use functions related to the moments of the distribution function, with $\Psi_0 = f_0 v^3$, $\underline{\Psi_1} = \underline{f_1} v^3$, and $\underline{\underline{\Psi_2}} = \underline{\underline{f_2}} v^3$. In this way, we can write Eqs. (8) and (9) as

$$\frac{\partial}{\partial \varepsilon}(S_\varepsilon \Psi_0) + e\frac{\partial}{\partial \varepsilon}\left(\underline{\Psi_1} \cdot \underline{E}\right) - \frac{S_\varepsilon}{2\varepsilon}\Psi_0 - \frac{e}{2\varepsilon}\underline{\Psi_1} \cdot \underline{E} = \underline{\nabla} \cdot \underline{\Psi_1} + \frac{\partial}{\partial \varepsilon}\left(S_\varepsilon \Psi_0^m\right) - \frac{S_\varepsilon}{2\varepsilon}\Psi_0^m, \tag{11}$$

$$\frac{\partial}{\partial \varepsilon}\left(S_\varepsilon \underline{\Psi_1}\right) + e\frac{\partial}{\partial \varepsilon}\left(\underline{\underline{\Psi_2}} \cdot \underline{E}\right) - \left(\frac{S_\varepsilon}{2\varepsilon} + \frac{\nu_{ee}+\nu_{ei}}{v}\right)\underline{\Psi_1} - \frac{e}{2\varepsilon}\left(\Psi_0 \underline{E} + v\underline{\Psi_1} \times \underline{B}\right) = \underline{\nabla} \cdot \underline{\underline{\Psi_2}}, \tag{12}$$

where $\underline{\underline{\Psi_2}} = \underline{\underline{\chi}}\Psi_0$.

By grouping the functions Ψ_l together into a vector $\underline{\Phi}$ and a second order tensor $\underline{\underline{F}}$, we can express these as matrix equations. Here, we simplify our expression and treat the situation in just two dimensions, such that

$$\underline{\Phi} = \begin{pmatrix} \Psi_0 \\ \Psi_{1,x} \\ \Psi_{1,y} \end{pmatrix}, \tag{13}$$

$$\underline{\underline{F}} = \begin{pmatrix} \Psi_{1,x} & \Psi_{1,y} \\ \Psi_{2,xx} & \Psi_{2,xy} \\ \Psi_{2,yx} & \Psi_{2,yy} \end{pmatrix}, \tag{14}$$

$$\frac{\partial}{\partial \varepsilon}\left[\left(S_\varepsilon \underline{\underline{I}} + \underline{\underline{M}}\right) \cdot \underline{\Phi}\right] - \underline{\underline{A}} \cdot \underline{\Phi} = \underline{\nabla} \cdot \underline{\underline{F}} + \underline{\Gamma_m}, \tag{15}$$

where

$$\underline{\underline{M}} \cdot \underline{\Phi} = e\left(\underline{\Psi_1} \cdot \underline{E}\Psi_0 \underline{\underline{\chi}} \cdot \underline{E}\right) = e\begin{pmatrix} 0 & E_x & E_y \\ \chi_{xx}E_x + \chi_{xy}E_y & 0 & 0 \\ \chi_{yx}E_x + \chi_{yy}E_y & 0 & 0 \end{pmatrix} \cdot \underline{\Phi}, \tag{16}$$

$$\underline{\underline{A}} = \frac{1}{2\varepsilon}\begin{pmatrix} S_\varepsilon & eE_x & eE_y \\ eE_x & S_\varepsilon & evB_z \\ eE_y & -evB_z & S_\varepsilon \end{pmatrix} + \frac{\nu_{ee}+\nu_{ei}}{v}\begin{pmatrix} 0 & 0 & 0 \\ 0 & 1 & 0 \\ 0 & 0 & 1 \end{pmatrix}, \tag{17}$$

and

$$\underline{\Gamma_m} = \begin{pmatrix} \left(\frac{\partial}{\partial \varepsilon} - \frac{1}{2\varepsilon}\right) S_\varepsilon \Psi_0^m \\ 0 \\ 0 \end{pmatrix}. \tag{18}$$

We solve these equations using energy as a pseudo-time variable, starting at the highest energy group and iterating down to the lowest energy group. If we choose a sufficiently high energy group to begin with, we can use the boundary condition $\underline{\Phi} \to \underline{0}$ as $\varepsilon \to \infty$. At each subsequent energy group g, we can then calculate the next iteration by solving the matrix equation

$$\frac{1}{\Delta\varepsilon}\left[\left(S_{g+1}\underline{\underline{I}} + \underline{\underline{M}}_g\right) \cdot \underline{\Phi}_{g+1} - \left(S_g \underline{\underline{I}} + \underline{\underline{M}}_g\right) \cdot \underline{\Phi}_g\right] - \underline{\underline{A}}_g \cdot \underline{\Phi}_g \approx \underline{\nabla} \cdot \underline{\underline{F}}_{g+1} + \underline{\Gamma_m}_g, \tag{19}$$

$$\left[\frac{S_g \underline{\underline{I}} + \underline{\underline{M}}_g}{\Delta\varepsilon} + \underline{\underline{A}}_g\right] \cdot \underline{\Phi}_g \approx \frac{S_{g+1}\underline{\underline{I}} + \approx \underline{\underline{M}}_g + 1}{\Delta\varepsilon} \cdot \underline{\Phi}_{g+1} - \underline{\nabla} \cdot \underline{\underline{F}}_{g+1} + \underline{\Gamma_m}_g. \tag{20}$$

At each energy group, this equation should be solved at every point in space. This calculation can be performed in parallel across the grid, as $\underline{\Phi}$ at each spatial point only depends on the neighboring points through the flux $\underline{F}$. However, we cannot calculate $\underline{\underline{M}}_g$ without knowing $\underline{\chi}g$. In this work, we assume that our energy groups are sufficiently close to one another and that $\underline{\underline{\chi}}$ is sufficiently slowly varying with energy that we can approximate $\underline{\underline{M}}_g \approx \underline{\underline{M}}_{g+1}$.

More generally, our energy groups must be closely spaced enough to resolve the frictional force exerted over one grid cell at any energy group. This gives the Courant–Friedrichs–Lewy (CFL) condition for a grid spacing Δx described by

$$\varepsilon_g - \varepsilon_{g-1} \le \left[S_\varepsilon(\varepsilon_g) - e\frac{\underline{\Psi_1}(\varepsilon_g) \cdot \underline{E}}{\Psi_0(\varepsilon_g)}\right]\Delta x. \tag{21}$$

If this condition is not met, the M1 equations are prone to numerical instability which takes the form of strong oscillations with a wavelength of twice the grid spacing. As the stopping power reduces at low collision rates or as the electric field increases for steep temperature or density gradients, this condition becomes more and more difficult to meet. Ultimately, this causes the code to crash in nonlocal conditions, where $\lambda_{\mathrm{mfp}} \nabla T_e/T_e$ becomes large.

3. Diffusive flux term

One approach to reducing oscillations and improving the resilience of the M1 solver is to add a diffusive term to the flux $\underline{\nabla} \cdot \underline{\underline{F}}$. This uses a Harten–Lax–van Leer (HLL) upstreaming scheme which defines the flux at spatial indices i and j (for x and y, respectively), as

$$\underline{F_{\mathrm{HLL},x}}\left(i+\frac{1}{2},j\right) = \frac{1}{2}\left[\underline{F_x}(i+1,j) + \underline{F_x}(i,j)\right] - \frac{1}{2}\left[\underline{\Phi}(i+1,j) - \underline{\Phi}(i,j)\right], \tag{22}$$

$$\underline{F}_{\mathrm{HLL},y}\left(i,j+\frac{1}{2}\right)=\frac{1}{2}\left[\underline{F}_y(i,j+1)+\underline{F}_y(i,j)\right]-\frac{1}{2}[\underline{\Phi}(i,j+1)-\underline{\Phi}(i,j)], \quad (23)$$

such that $\underline{\nabla}\cdot\underline{F}_{\mathrm{HLL}}=\underline{\nabla}\cdot\underline{F}-\Delta x\nabla^2\underline{\Phi}$, using a centered difference scheme with kernels of $[-0.5,0,0.5]$ and $[-0.5,1,-0.5]$ for $\underline{F}$ and $\underline{\Phi}$, respectively.

In practice, this means that minima and maxima in $\underline{\Phi}$ are damped out, by a term which looks like $\partial_\varepsilon[(S_\varepsilon\underline{I}+\underline{\underline{M}})\cdot\underline{\Phi}]=\ldots-\Delta x\nabla^2\underline{\Phi}$. This term plays the largest role when the grid cell size Δx and energy group spacing are both large, such that it can overwhelm simulations if we are not careful, causing unphysical results and crashes. Either the diffusive term should be turned off under these conditions or else the grid resolution should be increased and energy group spacing should both be reduced.

4. Reduced electric field

In some circumstances with strong temperature gradients, $e|\underline{E}|>S_\varepsilon$, meaning that it is impossible to meet the CFL condition described in Eq. (21). In these circumstances, the code will always crash, regardless of whether the diffusive term is used or the number of energy groups used. Here, an artificial reduction in the electric field experienced by higher energy groups can be used to stabilize the M1 code.

In order to ensure that the CFL condition is always achievable, with $S_\varepsilon>e\underline{E}\cdot\underline{\Psi}_{1x}/\Psi_0$, we use an energy dependent effective electric field, described by the harmonic mean of the field and the stopping power, as

$$\underline{E}_{\mathrm{red}}=\hat{\underline{E}}\left(\frac{1}{|E|}+\frac{e}{S_\varepsilon}\right)^{-1}. \quad (24)$$

This decreases the electric field sufficiently to ensure that the CFL condition can always be satisfied given enough energy groups, at a cost to the accuracy of the distribution function. It will unphysically decrease the electric field at high energy groups. Eventually, as ∇T_e increases or S_ε decreases, this will lead to changes in the crossover between outward and return current and will substantially change the final heat flow predicted by the model.

This process of decreasing the electric field prevents electrons from ever being accelerated by the field more than they are being decelerated by the collisional friction. This is a fundamental limitation of the current approach, where energy groups are solved iteratively downward, as causality here implies that each energy group is independent of lower energy electrons, with no heating possible. In future, iterative runs of the M1 code solver starting from both lower and upper boundaries and converging toward a consistent solution may help to overcome these limitations.

5. Ampère current condition

We have discussed how to calculate the electron distribution function for a given electric field, but actually the electric field is itself dependent on the electron distribution function. The system must, therefore, be solved self-consistently with the electric field chosen such that Maxwell's equations hold. Ampère's law imposes a constraint on $\underline{f}_1$ through the current. Retaining the quasi-static approximation, we have $\underline{J}=\mu_0\underline{\nabla}\times\underline{B}$. We calculate $\underline{J}$ from $\underline{f}_1$ assuming stationary ions as

$$\underline{J}=\int\int\int-f_e e\underline{v}\,v^2\mathrm{d}^2\Omega\mathrm{d}v=-e\int\underline{f}_1 v^3\mathrm{d}v. \quad (25)$$

In most situations that we model, with a uniform magnetic field, this becomes the zero-current condition $\underline{J}=\underline{0}$. We reach this condition by iteratively updating the electric field and the distribution function as follows:

1. For a given magnetic field, we calculate the target current as $\underline{J}_f=\mu_0\underline{\nabla}\times\underline{B}$.
2. We make an initial guess for the electric field $\underline{E}_0=-\frac{T_e}{n_e}\underline{\nabla}n_e-\xi\underline{\nabla}T_e$, where we use $\xi\equiv1+\frac{3}{2}\frac{Z+0.477}{Z+2.15}$.
3. For an electric field $\underline{E}_n$ at iteration n, we calculate the moments of the distribution function Ψ_{0n} and $\underline{\Psi}_{1_n}$, using Eq. (20).
4. We use $\underline{\Psi}_{1_n}=\underline{f}_{1_n}v^3$ to calculate the residual current $\underline{J}_n$ using Eq. (25).
5. We estimate the resistivity tensor $\underline{\underline{\eta}}$ and calculate the corresponding residual electric field $\underline{\Delta E}_n=\underline{\underline{\eta}}\cdot(\underline{J}_n-\underline{J}_f)$.
6. We repeat the process from step 3, using a new estimate for the electric field $\underline{E}_{n+1}=\underline{E}_n-\alpha\underline{\Delta E}_n$, for a controlled descent parameter α.
7. We terminate the process when the error in the current is small, below some chosen tolerance $|\eta_0||\underline{J}_n-\underline{J}_f|<\delta|\underline{E}_n|$ for a tolerance δ.

This process works well when the distribution function is close to Maxwellian, as $\underline{E}_0$ is a good estimate for the final self-consistent value for the electric field, and we can use a local Braginskii estimate for the resistivity $\underline{\underline{\eta}}$. As the distribution function becomes further from a Maxwellian, however, the system has to perform more iterations to get close to the self-consistent electric field and also the accuracy of the improvement $\underline{\Delta E}_n$ gets worse as the estimate for the resistivity breaks down.

One solution is to use a secant approximation for finding the root, using the measured transformation $(\underline{E}_n-\underline{E}_{n-1})=\underline{\underline{\eta}}_n\cdot(\underline{J}_n-\underline{J}_{n-1})$. For a resistivity tensor described by $\underline{\underline{\eta}}=\begin{pmatrix}\eta_\perp & \eta_\wedge\\ -\eta_\wedge & \eta_\perp\end{pmatrix}$ in the plane perpendicular to the magnetic field, we can show that

$$\eta_{\perp,n}=\frac{(\underline{E}_n-\underline{E}_{n-1})\cdot(\underline{J}_n-\underline{J}_{n-1})}{|\underline{J}n-\underline{J}n-1|^2}, \quad (26)$$

$$\eta_{\wedge,n}=\frac{|(\underline{E}_n-\underline{E}_{n-1})\times(\underline{J}_n-\underline{J}_{n-1})|}{|\underline{J}n-\underline{J}n-1|^2}. \quad (27)$$

Iteratively improving our guess for $\underline{\underline{\eta}}_n$ using the measured change in the current improves the rate of convergence toward the target current. To avoid issues with convergence near $\underline{\Delta E}_n=(\underline{J}_n-\underline{J}_{n-1})=\underline{0}$, we smooth the resistivity tensor over a spatial scale chosen to match the scale of the problem.

C. hybrid-AWBS-BGK code

We wish to compare M1 predictions with the hybrid-AWBS-BGK code developed by Milan Holec and built upon the powerful MFEM framework.[31] In a similar manner to M1, this solves the equations for the moments of the distribution function (8) and (9) by integrating from the highest energy group downward. As with the M1 model, it assumes a quasi-static situation with $\partial_t f_e \ll (\partial_t f_e)_{\text{coll}}$ and adjusts the electric field until reaching the zero current condition. However, it uses the P1 closure $\underline{\underline{f_2}} = f_0 \underline{\underline{I}}/3$, which makes the code more robust but possibly less accurate at high non-localities.

hybrid-AWBS-BGK has the option to run with either AWBS or BGK collision operators for f_1, but always uses the BGK collision operator for f_0. In most of this work, we used BGK collisions for both f_0 and f_1, which made the solver more robust at long mean free paths and high degrees of non-locality. This takes the form of

$$\left(\frac{\partial f_e}{\partial t}\right)^{\text{BGK}}_{\text{coll}} = -\nu_{ee}(f_e - f_e^m) + \frac{\nu_{ee}+\nu_{ei}}{2}\frac{\partial^2}{\partial \Omega^2} f_e. \tag{28}$$

Note that currently hybrid-AWBS-BGK does not separately calculate the electron and ion collision frequencies, instead using an estimated total collision frequency $\nu_{ei} + \nu_{ee} \approx \nu^* \equiv \nu_{ei}(Z + 4.2)/(Z + 0.24)$. At sufficiently high Z, the error from this approximation is on the level of a few percent.

In order to converge to the self-consistent electric field, hybrid-AWBS-BGK also applies the Ampère current condition, but here the magnetic field is kept constant over the domain, forcing the target current to $\underline{J} = \underline{0}$. The electric field is, therefore, adjusted after each iteration to minimize the current.

D. Vlasov–Fokker–Planck codes

We compare all the models against full Vlasov–Fokker–Planck simulations performed with the codes IMPACT[22] and K2.[23] These also calculate the f_0 and f_1 moments of the distribution function over multiple energy groups, but are time-dependent codes, where the temperature evolves dynamically in response to the heat flow. In this way, the code calculates how all energy groups of the distribution function evolve over time from an initially isotropic thermal distribution to a self-consistent solution. There is, however, not necessarily a converged steady state, as the system relaxes toward a uniform temperature with no temperature gradients or heat flow. The heat flow profile is therefore recorded when the thermal conductivity has converged, such that the ratio of the predicted heat flow to the diffusive heat flow is constant. This gives a close-to-converged solution for a temperature profile close to the initial conditions.

These VFP codes treat the problem slightly differently; whereas IMPACT uses an implicit solver in time, with large timesteps, K2 is explicit, with timesteps by necessity less than the electron cyclotron period $2\pi/\omega_c = 2\pi m_e/eB$. K2 includes both electron inertia ($\partial f_e/\partial t \neq 0$) and electron–electron collisions, while IMPACT has electron inertia turned off and uses the same approximation for the combined electron–electron and electron–ion collision frequency as hybrid-AWBS-BGK.

The normalisations of each of these codes are also different. M1 and K2 are written using SI units for space, density, and heat flow, with temperature in electronvolts and magnetic field in tesla. hybrid-AWBS-BGK uses cgs units, taking temperature in electronvolts and magnetic field in terms of the Larmor frequency $\omega_c = eB/m_e$.

IMPACT, on the other hand, uses a set of normalized units, with velocity given in terms of a base temperature T_{e0} as $v_n = \sqrt{2eT_{e0}/m_e}$, time in terms of the corresponding Spitzer electron–ion collision time $\tau_n = v_n^3(4\pi\varepsilon_0/e^2)^2/4\pi Z_0 n_{e0} \ln\Lambda_{ei0}$, and lengths in terms of the thermal mean free path $\lambda_n = v_n\tau_n$. Again, the Coulomb logarithm is constant across the entire simulation. The density must be given relative to n_{e0} and the magnetic field must be given as the thermal Hall parameter $\omega_c\tau_n$. The heat flow is also returned in terms of $q_n = m_e n_{e0} v_n^3$. Furthermore, the moments of the distribution function are scaled differently in IMPACT such that $f_e = f_0' + \underline{f_1'}\cdot\hat{\underline{v}}$. This gives $f_0' = 4\pi f_0$ and $\underline{f_1'} = (4\pi/3)\underline{f_1}$, with the distribution function given in terms of $f_n = n_{e0}/v_n^3$.

E. Local models

We wish to compare the predictions of the M1 model with the local, diffusive models developed by Spitzer–Härm,[30] Braginskii,[9] and Epperlein–Haines.[10] All of these models calculate the heat flow for a plasma with $f_0 \approx f_0^m$. This gives a heat flow at any given point determined purely by the plasma parameters at that point, i.e., it is "local." In order to express the $\underline{f_1}$ part of the distribution function analytically, we have gone further and used the Lorentz gas approximation, considering only angular scattering as

$$\left(\frac{\partial f_e}{\partial t}\right)_{\text{coll}} = \frac{\nu_{ee}+\nu_{ei}}{2}\frac{\partial^2}{\partial\Omega^2} f_e. \tag{29}$$

1. Spitzer-Härm

With both the Spitzer–Härm and the Lorentz gas approximations, calculated for $\underline{B} = 0$, the $\underline{f_1}$ moment of the distribution function can then be calculated analytically from Eq. (9) if we use a P1 closure of $\underline{\underline{f_2^{\text{SH}}}} = f_0^m \underline{\underline{I}}/3$ and use an electric field given by $\underline{E} = -\xi\underline{\nabla} T_e$. If the electron density is constant, this gives an estimate for $\underline{f_1^{\text{SH}}}$ given by

$$\underline{f_1^{\text{SH}}} = -\left(\frac{v^2}{v_{\text{th}}^2} - 3 - 2\xi\right)\frac{v f_0^m}{6(\nu_{ee}+\nu_{ei})}\frac{\underline{\nabla} T_e}{T_e}. \tag{30}$$

This expression shows the basic form for the electron distribution, with hot electrons flowing down the temperature gradient, countered by a return current for $v < \sqrt{3+2\xi}v_{\text{th}}$. If we further approximate the Coulomb logarithms $\ln\Lambda_{ee}$ and $\ln\Lambda_{ei}$ as independent of velocity, this expression can be integrated over velocity as per Eq. (5) to give the Spitzer–Härm heat flow

$$\underline{q^{\text{SH}}} = -20\delta_T\varepsilon\left(\frac{2}{\pi}\right)^{\frac{3}{2}}\left(\frac{4\pi\varepsilon_0}{e^2}\right)^2\frac{e^{\frac{7}{2}}T_e^{\frac{5}{2}}\underline{\nabla} T_e}{m_e^{\frac{1}{2}}(Z\ln\Lambda_{ei}+\ln\Lambda_{ee})}, \tag{31}$$

where $\delta_T\varepsilon = (7-2\xi)/5$ describes the impact of the electric field contribution to the heat flow. Spitzer further shows that if the electric field is allowed to evolve in order to reach $\underline{J} = \underline{0}$, then $\xi = \frac{5}{2}$ and $20\delta_T\varepsilon = 8$.

2. Braginskii and Epperlein–Haines

Braginskii and Epperlein–Haines both go further than Spitzer, in permitting a magnetic field $\underline{B} \neq \underline{0}$. If we again use the Lorentz approximation to reduce collisions to just angular scattering, this changes the form of the first moment of the distribution function as

$$\underline{f_1^{\mathrm{B}}} = \frac{1}{1+\chi^2}\left(\underline{f_1^{\mathrm{SH}}} - \chi \underline{f_1^{\mathrm{SH}}} \times \underline{\hat{B}}\right) + \left(\underline{f_1^{\mathrm{SH}}} \cdot \underline{\hat{B}}\right)\underline{\hat{B}}, \tag{32}$$

where $\chi = \omega_c/(\nu_{ei}+\nu_{ee})$ is the Hall parameter, the ratio of the cyclotron frequency to the collision frequency. The first term in the brackets represents the reduction in the flow of electrons down temperature gradients due to magnetization (with higher velocity electrons more strongly magnetized). The second term describes the Righi–Leduc flow, perpendicular to both the temperature gradient and the magnetic field. The third term describes the flow along magnetic field lines, which we will generally neglect in the rest of this work, in order to focus on transport perpendicular to the magnetic field.

It is also worth emphasizing that a magnetic field changes the electric field. Because χ is a function of particle velocity, reaching zero current in $\underline{f_1^{\mathrm{SH}}}$ does not ensure zero current in $\underline{f_1^{\mathrm{B}}}$. Instead, the electric field must be described by $\underline{E} = -\underline{\underline{\xi}} \cdot \underline{\nabla} T_e$ for a tensor $\underline{\underline{\xi}}$ in order to ensure Ampère's law is satisfied in all directions.

Crucially, Eq. (32) means that the heat flow can no longer be calculated analytically, due to the velocity and Z dependence in the Hall parameter. Instead, the heat flow is calculated by means of fits to the integrated solution of the linearized Fokker–Planck equation. Braginskii first performed these fits over a range of Hall parameters for a given set of ionization states, and Epperlein and Haines subsequently improved the fitting agreement and performed the integrations over a wider range of ionization states.

In the Braginskii fits, the heat flow perpendicular to the magnetic field is described by

$$\underline{q^{\mathrm{B}}} = -\kappa_{\perp}^{\mathrm{B}} \underline{\nabla} T_e - \kappa_{\wedge}^{\mathrm{B}} \underline{\hat{B}} \times \underline{\nabla} T_e, \tag{33}$$

where

$$\kappa_{\perp}^{\mathrm{B}} = \frac{\gamma_0' + \gamma_1' \chi_B^2}{\delta_0 + \delta_1 \chi_B^2 + \chi_B^4} \frac{n_e e^2 T_e}{m_e} \tau_B, \tag{34}$$

$$\kappa_{\wedge}^{\mathrm{B}} = \chi_B \frac{\gamma_0'' + \gamma_1'' \chi_B^2}{\delta_0 + \delta_1 \chi_B^2 + \chi_B^4} \frac{n_e e^2 T_e}{m_e} \tau_B, \tag{35}$$

$$\tau_B = \frac{3}{4\sqrt{2\pi}} \frac{\sqrt{m_e}(eT_e)^{\frac{3}{2}}}{Z n_e \ln \Lambda_{ei}}, \tag{36}$$

$\chi_B = \omega_c \tau_B$ is the Hall parameter for the Braginskii thermal collision time τ_B, and γ_0', γ_1'', and δ_0 are the fitting parameters as functions of Z. These are given below for low Z, where $\nu_{ei} \approx \nu_{ee}$, and for high Z, where $\nu_{ei} \gg \nu_{ee}$,

Z	γ_0'	γ_1'	γ_0''	γ_1''	δ_0	δ_1
1	11.92	4.664	21.67	2.50	3.7703	14.79
∞	1.20	3.25	10.23	2.50	0.0961	7.482

In the Epperlein–Haines fits, the heat flow perpendicular to the magnetic field takes the same form, but with different conductivities described by

$$\underline{q^{\mathrm{EH}}} = -\kappa_{\perp}^{\mathrm{EH}} \underline{\nabla} T_e - \kappa_{\wedge}^{\mathrm{EH}} \underline{\hat{B}} \times \underline{\nabla} T_e, \tag{37}$$

where

$$\kappa_{\perp}^{\mathrm{EH}} = \frac{\gamma_0' + \gamma_1' \chi_B}{c_0' + c_1' \chi_B + c_2' \chi_B^2 + \chi_B^3} \frac{n_e e^2 T_e}{m_e} \tau_B, \tag{38}$$

$$\kappa_{\wedge}^{\mathrm{EH}} = \chi_B \frac{\gamma_0'' + \gamma_1'' \chi_B}{c_0'' + c_1'' \chi_B + c_2'' \chi_B^2 + \chi_B^3} \frac{n_e e^2 T_e}{m_e} \tau_B, \tag{39}$$

where for high and low Z the fitting parameters are given below:

Z	γ_0'	γ_1'	c_0'	c_1'	c_2'	γ_0''	γ_1''	c_0''	c_1''	c_2''
1	6.18	4.66	1.93	2.31	5.35	4.01	2.5	0.661	0.931	2.50
∞	6.21	3.25	0.457	4.81	8.53	0.186	2.5	0.001	0.018	0.43

III. COMPARISON IN LOCAL REGIME

A. Non-magnetized results

Starting with the simplest case of a one-dimensional weak temperature gradient in an otherwise uniform collisional plasma with no magnetic field, we wish to verify that all of our codes are working correctly. We start at a high density of $n_{e0} = 10^{21}\,\mathrm{cm}^{-3}$, with a background temperature of $T_{e0} = 300\,\mathrm{eV}$ and an ionization state of $Z = 100$. $B = 0$ throughout. For a thermal velocity $v_{\mathrm{th}} = \sqrt{eT_{e0}/m_e} = 7.26 \times 10^6\,\mathrm{m/s}$, we use the NRL definitions of the thermal Coulomb logarithm[32] to calculate $\nu_{ee} = 11.6\,/\mathrm{ps}$ and $\nu_{ei} = 582\,/\mathrm{ps}$, giving a mean free path of $\lambda_{ei,\mathrm{th}} = 12.5\,\mathrm{nm}$. We model a small tanh perturbation to the temperature, taking the following form:

$$T_e(x) = T_{e0} + \Delta T_e \tanh(kx), \tag{40}$$

with $\Delta T_e = 3\,\mathrm{eV}$ and $k = 2\pi \times 10^3\,/\mathrm{m}$. This gives $k\lambda_{ei,\mathrm{th}} = 7.8 \times 10^{-5}$ and a peak Knudsen number of $K_n = \lambda_{ei,\mathrm{th}} \nabla T_e / T_e = \lambda_{ei,\mathrm{th}} k \Delta T_e / T_{e0} = 7.8 \times 10^{-7}$, such that the transport is in the local regime in both respects.

M1 simulations are performed using a spatial grid spanning $\pm 1\,\mathrm{mm}$ with 101 grid points giving $\Delta x = 20\,\mu\mathrm{m}$. We use a linearly spaced energy grid from 6 eV up to 600 eV with 500 energy groups. At this high density, the minimum stopping power is $S_\varepsilon = 1.18 \times 10^7\,\mathrm{eV/m}$, giving a CFL condition of $\Delta E \leq 237\,\mathrm{eV}$, which is easily exceeded. We turn the diffusive term off such that $\underline{\underline{F_{\mathrm{HLL}}}} = \underline{\underline{F}}$.

Figure 1 shows the temperature profile, the resulting electric field, and some of the results of the M1 simulations. In the local regime, the initial guess for the electric field is very good and the code converges to the zero-current condition in just five iterations, taking 2.1 s on a single processor. The first moment of the distribution function, plotted as Ψ_{1x}, shows the flow of high energy electrons down the temperature gradient, countered by a return current driven by the electric field.

M1 gives us an estimate for the entire distribution function and we can, therefore, compare the moments of the distribution function calculated by the M1 simulation to the analytic predictions described

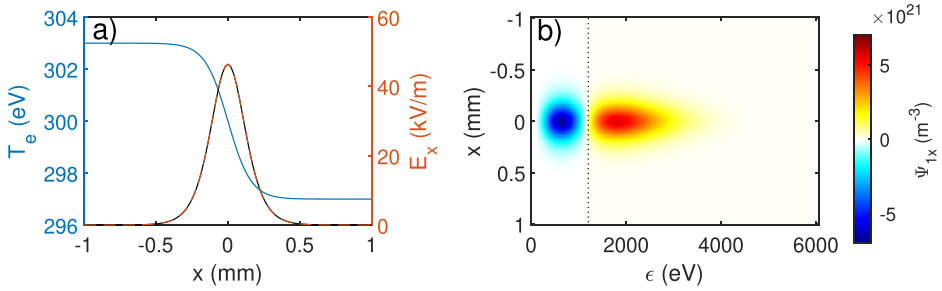

FIG. 1. (a) Temperature profile for the ramp test problem (blue) and the resulting electric field. The initial profile calculated from the temperature gradient (solid black) is compared with the result after convergence to zero current (dashed red). (b) The first moment of the distribution function calculated using the M1 code, shown as Ψ_{1x} plotted against energy and space. The black dotted line at $\epsilon = 4T_{e0}$ marks the transition between outward flow and return current.

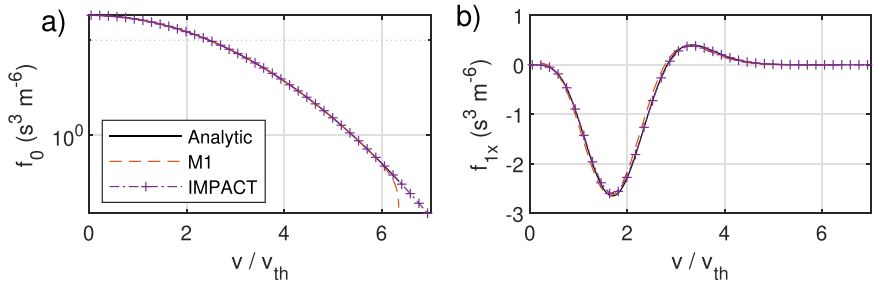

FIG. 2. (a) The zero-th moment of the distribution function $f_0(v)$ in a non-magnetized plasma at $x = 0$ predicted by M1 (dashed red), compared with the analytic form $f_0^m(v)$ (solid black) and with IMPACT (dash-dot purple). (b) The first moment of the distribution function at $x = 0$, again comparing the prediction from M1 with the analytic estimate $f_{1x}^{SH}(v)$ and with IMPACT (same color scheme).

in Eqs. (6) and (30) and to the results of an IMPACT simulation. The IMPACT simulation was run with 80 energy groups for 400 collision times until the heat flow reached a steady state, taking around 7 min on four processors, and the moments of the distribution function were converted to match the forms shown in Eqs. (2)–(4), rather than the IMPACT forms. The results are shown in Fig. 2, demonstrating excellent agreement across the whole distribution function. As expected, the zeroth moment predicted by the M1 model diverges from the analytic estimate f_0^m only at the highest energy group, where we assumed $f_0 = 0$ as $v \to \infty$. The first moment of the distribution function, on the other hand, matches fairly well throughout but does show signs of a lag in the simulation, where the M1 curve is slightly to the left of the analytic prediction. Both curves, however, cross the x axis within 2% of $v = \sqrt{8}v_{th}$.

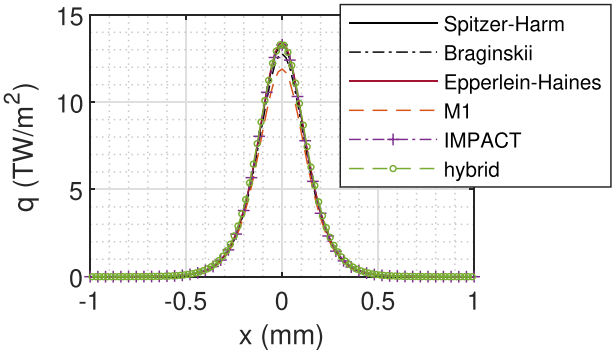

FIG. 3. Heat flow profiles in an unmagnetized plasma predicted by each of the three local models and three multi-group models. IMPACT and hybrid-AWBS-BGK results have been calculated accordingly from the normalized units.

Finally, we can compare the heat flows predicted by each of the different models, shown in Fig. 3. IMPACT results were taken from the run shown in Fig. 2, while hybrid-AWBS-BGK was run using the BGK collision operator with 80 energy groups and third order grid refinement within each cell. Results from all of the models lie close to one another, within 15%. Spitzer–Härm, Epperlein–Haines, and IMPACT results lie particularly close, such that they are close to indistinguishable. Braginskii's fits perform slightly worse here, as the fits were carried out at low Z or at $Z = \infty$, rather than close to $Z = 100$.

M1 slightly underpredicts the heat flow by around 10%, likely due to the slight lag seen in Fig. 2. Convergence testing shows that using more energy groups does lead to a slight reduction in the lag and a slight increase in the heat flow, but still not by enough to match the other models. The heat flow predicted by hybrid-AWBS-BGK is slightly closer to the local predictions, within 3%, with a runtime of just 20 s.

B. Magnetized results

Satisfied that the M1 model is working in the local regime and that the correct normalisations are being used to compare all of the models, we consider the effect of a uniform magnetic field. Using the same conditions as Sec. III A and the same temperature profile described by Eq. (40), we introduce a constant magnetic field B_z with an amplitude from 3 T up to 3×10^4 T. In this highly collisional regime, this explores Hall parameters in the range $\chi_B = 10^{-2} - 10^2$.

Examples of the electric field and the Ψ_{1x} and Ψ_{1y} moments of the distribution function for a magnetized plasma at a Braginskii Hall parameter of $\chi_B = 0.14$ are shown in Fig. 4. The high energy end of the distribution function is suppressed by $1/(1 + \chi^2)$ as described in Eq. (32). This means a lower electric field parallel to the temperature gradient is required to achieve $J_x = 0$, resulting in a smaller return

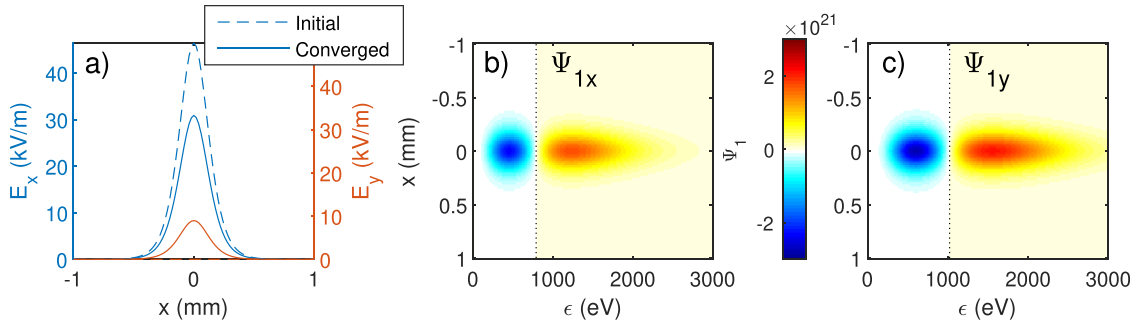

FIG. 4. (a) Electric fields in a magnetized plasma at the initial guess (dashed) and after convergence to the zero-current condition (solid), shown as components parallel to the temperature gradient (E_x, blue) and perpendicular to both the temperature gradient and the magnetic field (E_y, red). (b) and (c) Components of the distribution function, plotted as Ψ_{1x} (b) and Ψ_{1y} (c) on the same color scale. The crossover between return current and outward current is marked by a dotted black line.

current. The crossover is now at $\varepsilon = 2.6T_{e0}$ and moves to lower energies as the Hall parameter increases.

Perpendicular to the temperature gradient, however, a strong component of the distribution function is present, with $\Psi_{1y} > \Psi_{1x}$ even with $\chi_B < 1$. Ensuring $J_y = 0$ now requires an electric field perpendicular to the temperature gradient, with a return current below $\varepsilon = 3.4T_{e0}$. The dependence on $\chi/(1+\chi^2)$ means this component of the distribution function tends to dominate at high energies. The equivalent $\underline{\underline{\xi}}$ tensor is given by $\underline{E} \approx -\begin{pmatrix} 1.7 & -0.5 \\ 0.5 & 1.7 \end{pmatrix} \cdot \underline{\nabla} T_e$.

We compare the predictions from the different models over a range of Hall parameters by plotting the peak heat flows predicted by each model, taken at $x = 0$, against the Braginskii Hall parameter $\chi_B = \omega_c \tau_B$ in Fig. 5. All models are largely consistent in their predictions, but there are some significant variations. M1 predicts a Righi–Leduc heat flux around 20% too low at low Hall parameters, whereas Braginskii predicts a peak Righi–Leduc heat flow around 20% higher than Epperlein–Haines. Despite these variations, the M1 model performs well over a wide range of parameters and is particularly close to IMPACT and Epperlein–Haines fits at $\chi_B > 0$, where the predicted heat flows are all within a few percent. Once again, the results from the hybrid-BGK model match the Epperlein–Haines fits very well.

IV. NON-LOCALITY

A. Ramp test

Now we have demonstrated the reliability of the M1 model in the local regime, we wish to use it to test the divergence of heat flow in less collisional regimes. We maintain the same temperature profile and change the collisionality by reducing the density n_e. However, to simplify the situation, we keep the Coulomb logarithms constant at $\ln \Lambda_{ee} = \ln \Lambda_{ei} = 6$. With this assumption, the heat flow predicted by the local models is constant with density, such that any divergence from the original heat flow profile is caused by nonlocal effects.

As the density and collision frequency falls, the CFL condition becomes increasingly stringent and more energy groups are required. Running the M1 code at a density of 3×10^{18} cm^{-3} requires 300 000 energy groups, taking 63 min to reach convergence on a single processor. However, including the diffusive term $-\nabla^2 \underline{\Phi}$ in the HLL flux and using zero-gradient boundary conditions for f_1 ($\partial_x f_1(|x| = x_{\max}) = 0$) stabilizes the code against oscillations in $\underline{\Phi}$ and allows the code to run with just 10 000 energy groups, taking 103 s. This does result in a loss in accuracy, however, with the peak heat flow reduced by around 10% compared to the non-diffusive value. The `hybrid-AWBS-BGK` code, on the other hand, takes over 15 min under these conditions.

Figure 6 shows the resulting distribution function and heat flow. The divergence from the local predictions shown in Fig. 1 are most visible off-axis, where the distribution function is much wider than before. The electric field is also significantly different to the initial Maxwellian prediction, with a lower field in the center and a higher field off-axis. The crossover point between outward-going and return current is much lower in the center, below 1000 eV, and much higher off-axis. This corresponds with a reduction in the heat flow in the center, due to flux-limitation, and an increase in the heat flow away from the steep temperature gradient, caused by pre-heat.

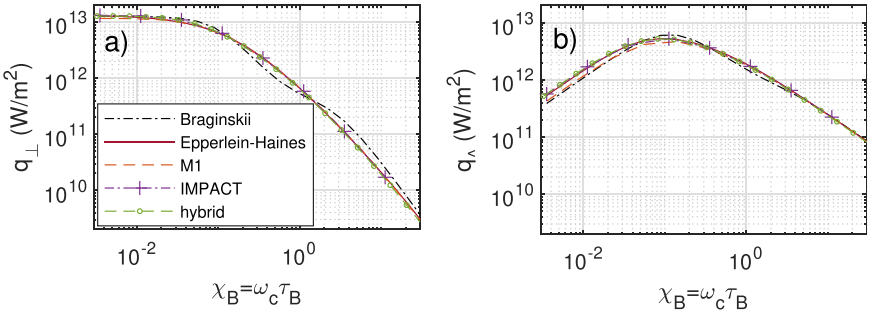

FIG. 5. Peak heat flows predicted by each model perpendicular to the magnetic field in a magnetized plasma in the local regime, plotted against the magnetic field strength shown through $\chi_B = \omega_c \tau_B$. Panel (a) shows the heat flow parallel to the temperature gradient, while panel (b) shows the Righi–Leduc heat flow perpendicular to both the temperature gradient and the magnetic field.

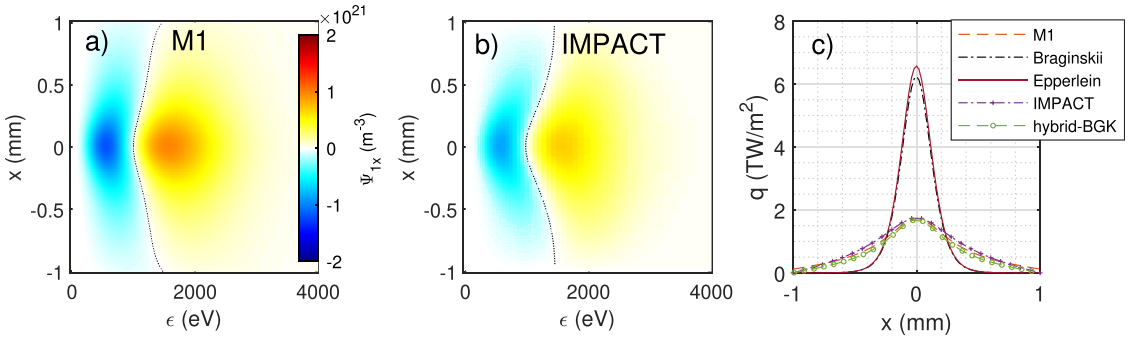

FIG. 6. (a) and (b) First moments of the distribution function Ψ_{1x} estimated by M1 (a) and by IMPACT (b) for the same tanh temperature profile as before, now at $n_e = 3 \times 10^{18}$ cm^{-3}. The contour where $\Psi_{1x} = 0$ is marked with a black dotted line and the color scale is the same for both plots. (c) Comparison of the heat flow profiles predicted by the different local models and by the multi-group models.

The predictions from M1 agree well with those from both hybrid-BGK and IMPACT. The increase in the distribution function off-axis and the shift to lower energies in the crossover point between return- and outward-current in the center are apparent in both M1 and IMPACT simulations. These result, respectively, in the increase in the heat flow away from the center and the suppression in peak heat flow, which match in all simulations and show large divergences from the Braginskii model. There are some differences between the different models, with M1 predicting a more uniform electric field across the temperature gradient and hybrid-BGK predicting very slightly lower heat flow in the wings. The zero-gradient boundary conditions for M1 also change the crossover between return- and outward-current at the boundary and give a small but finite heat flux at the boundary.

In order to study the differences between the models over a range of collisionalities, the peak heat flows are plotted against the Knudsen number $K_n = \lambda_{th} \nabla T_e / T_e$ for a range of collision frequencies in Fig. 7. Note that the hybrid-BGK calculations accounted for the change in Coulomb logarithm, recalculating the equivalent Braginskii heat flow for each simulation at the relevant Coulomb logarithm.

All of the multi-group models predict a reduction from the local heat flow beginning from $K_n \approx 10^{-6}$ upwards, with the heat flow dropping off such that it never exceeds a fraction of 1% of the free streaming limit in these simulations. There are, however, some

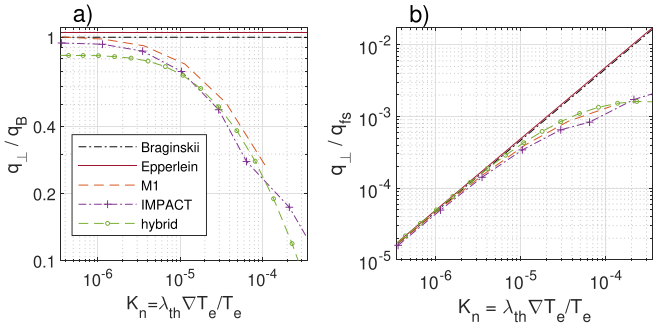

FIG. 7. (a) Peak heat flows predicted by the different models plotted against the Knudsen number. Decreasing collisionality is to the right. (b) Peak heat flows relative to the free-streaming limit $q_{fs} = n_e e T_e v_{th}$, again plotted against the Knudsen number.

significant differences between the model predictions in the non-local regime. M1 predicts heat flows up to 30% higher than IMPACT, although some of this will be due to relaxation in the temperature profile in the IMPACT simulations. hybrid-BGK underpredicts the heat flow compared to local models at high collisionalities and begins to predict lower heat flows than IMPACT above a Knudsen number of 10^{-4}. This is likely due to the limitations of the P1 closure and it seems likely that hybrid-BGK will continue to underpredict heat flow.

On the other hand, the M1 code crashed for a Knudsen number greater than 10^{-4}, with the stopping power S_ε becoming smaller than the electric field due to the temperature gradient. Under these conditions, the reduced electric field must be used, using the harmonic mean of E and S_ε/e as described in Sec. II B 4.

B. Cosine test

We can instead look at a cosine perturbation with an arbitrarily small amplitude as $T_e(x) = T_{e0} + \Delta T_e \cos(kx)$. This keeps the electric field small and maintains $|f_1| \ll f_0$ but still demonstrates non-local behavior when $k\lambda_{th}$ becomes large and hot electrons can travel more than one wavelength between collisions.

Figure 8 shows the results of running simulations using M1, IMPACT, and hybrid-BGK with $T_{e0} = 300$ eV and $k = 2\pi \times 10^3$ as before. $\Delta T_e / T_{e0} = 10^{-4}$, $n_e = 10^{19}$ cm^{-3}, and $Z = 100$. Here, the mean free path of electrons with velocity $v_{th} = \sqrt{eT_e/m_e}$ is $\lambda_{th} = 1.2\,\mu$m. Although $k\lambda_{th} \approx 3.6 \times 10^{-3}$ is still small, hot electrons with $v = 3v_{th}$ travel a significant fraction of a wavelength before colliding. This blurs out the distribution function at high energies and greatly suppresses the heat flow even when the temperature gradient itself is small.

The distribution functions from M1 and IMPACT reflect this, showing the outward-going and return current contributions to Ψ_{1x} following the same sine profile as ∇T_e but with a lower amplitude. In IMPACT, this amplitude is reduced slightly further as the temperature profile relaxes toward equilibrium. This blurring of the distribution function results in heat flow predictions from both M1 and IMPACT which are much lower than the local diffusive Braginskii model.

Furthermore, for a cosine test, we can compare to previous descriptions for the reduction in heat flow made by Epperlein and Short[33] by fitting to results from VFP simulations. This predicts a

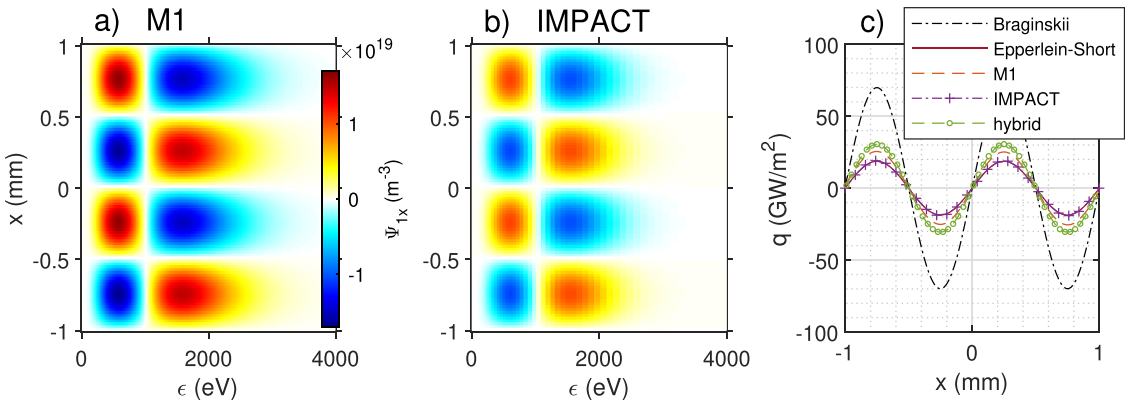

FIG. 8. (a) and (b) First moments of the distribution function Ψ_{1x} estimated by M1 (a) and by IMPACT (b) for the cosine test problem at $n_e = 10^{19}\,\mathrm{cm}^{-3}$. The color scale is the same for both plots. c) Heat flow profiles predicted by the different local models and by the multi-group models, compared with the prediction by Epperlein–Short.

reduction in heat flow by $q_{ES}/q_{SH} = [1 + (30k\lambda^*_{th})^{\frac{4}{3}}]^{-1}$, where $\lambda^*_{th}/\lambda_{th} = [(Z+1)(Z+0.24)/4.2Z(1+0.24Z)]^{\frac{1}{2}}$.

The heat flow predicted by IMPACT agrees closely with the Epperlein–Short prediction, which is reassuring. The heat flow predicted by the M1 model is close, but 30% higher, as the temperature profile is treated as entirely static here and cannot relax as in the VFP simulations. The heat flow predicted by hybrid-AWBS-BGK is significantly higher (60%) than the predictions from IMPACT, although this is largely due to the lower Coulomb logarithm used by this code (4.15 rather than 6 for all the other simulations).

The peak heat flow is plotted against $k\lambda_{th}$ for densities of $10^{16-21}\,\mathrm{cm}^{-3}$ in Fig. 9. Again, the hybrid-BGK calculations accounted for the change in Coulomb logarithm, recalculating the equivalent Braginskii heat flow for each simulation at the relevant Coulomb logarithm. This shows the same trend as in the ramp test, with M1 predicting heat flows dropping off rapidly as the mean free path increases above $k\lambda_{th} = 10^{-3}$. The heat flow predicted by M1 falls to 3% of the heat flow predicted by Braginskii at $k\lambda_{th} = 0.03$. For densities lower than $10^{18}\,\mathrm{cm}^{-3}$, however, the M1 simulations crashed regardless of how many energy groups were used, with no estimate for situations with $k\lambda_{th} \geq 0.1$. Beyond this point, the current M1 model is ineffective even with $f_1 \ll f_0$.

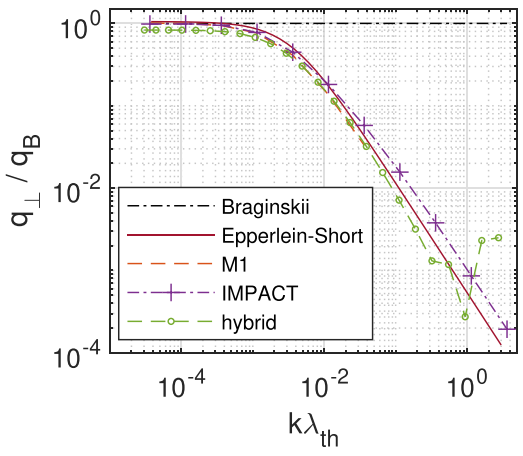

FIG. 9. Peak heat flows for the cosine test predicted by the different models, plotted against $k\lambda_{th}$. Decreasing collisionality is to the right.

We can also compare the predictions of the M1 model to the Epperlein–Short model over a range of $k\lambda_{th}$. This predicts that the heat flow falls away from the local prediction for $k\lambda_{th} > 10^{-3}$, ultimately proportional to $(k\lambda_{th})^{-\frac{4}{3}}$. The M1 predictions match well to Epperlein–Short over a wide range of $k\lambda_{th}$, although M1 systematically underestimates the heat flow relative to Epperlein–Short by $5\% - 25\%$. IMPACT simulations also match up well at $k\lambda_{th} < 0.1$, although in the most non-local situations IMPACT over-estimates the heat flow relative to Epperlein–Short by almost a factor of 2. hybrid-AWBS-BGK is very robust and works even up to $k\lambda_{th} = 1$, but then breaks down.

C. Magnetization

We were also interested in seeing the effect of a magnetic field on heat flow in the non-local regime. We used M1 and hybrid-BGK to run the linear cosine test problem at a selection of densities, corresponding to a local regime at $n_e = 10^{21}\,\mathrm{cm}^{-3}$, with $k\lambda_{th} = 3.6 \times 10^{-5}$, and increasingly non-local regimes, with $k\lambda_{th} = \{0.0036, 0.011, 0.036\}$. At greater degrees of non-locality than this the M1 simulations crashed with 10 000 groups. The heat flows for hybrid-BGK were scaled by the Coulomb logarithm to ensure consistency at the same value of $k\lambda$. Unfortunately, benchmarking against IMPACT simulations was not possible, as no convergence was achieved in the cross-gradient Righi–Leduc heat flow, and so the explicit VFP code K2 was used in its place. K2 could only reach convergence at fields up to $\chi_B = 10$. As the effect of magnetization is weakest for the highest energy groups, the cross-gradient heat flow depends more strongly on the very high energy components of the distribution function, which take longer to reach convergence.

With no magnetic field present, the resulting heat flows are significantly reduced relative to the local predictions, down to around 3% of the Epperlein–Haines prediction. Applying a magnetic field, however, changes the heat flow, both by restricting heat flow perpendicular to the magnetic field and by introducing a Righi–Leduc term perpendicular to the temperature gradient. A range of field strengths were modeled, chosen such that the Hall parameter was in the range $10^{-3} - 10^2$

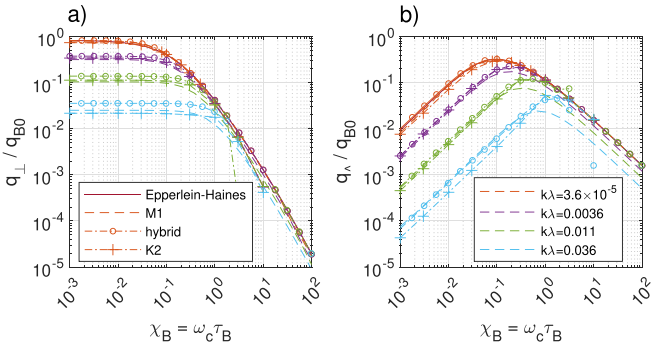

FIG. 10. Peak heat flows perpendicular to a magnetic field predicted by M1 (dashed lines) and hybrid-BGK (dashed circles) and by the VFP code K2 (dash-dot x's), compared to the Epperlein–Haines prediction in the local regime (solid) for a magnetized linear cosine test. The heat flows relative to the unmagnetised Braginskii heat flow q_{B0} are plotted against the Hall parameter for a range of different densities for (a) perpendicular transport, parallel to the temperature gradient, and (b) Righi–Leduc transport, perpendicular to both the magnetic field and the temperature gradient. Both legends apply to both panels.

for each of the plasma densities, requiring much higher field strengths at high densities. The resulting heat flows, both down the temperature gradient and the Righi–Leduc flow perpendicular to the temperature gradient, are shown in Fig. 10, plotted against the Hall parameter.

In all cases, increasing the magnetic field strength reduces the heat flow down the temperature gradient, with Hall parameters above 10^{-1} resulting in a strong reduction in the heat flow down the temperature gradient. On the other hand, increasing the magnetic field increases the Righi–Leduc heat flow perpendicular to the temperature gradient, as described earlier. At high $k\lambda_{\text{th}}$, the heat flow both parallel and perpendicular to the temperature gradient is already suppressed relative to the prediction without any magnetic field, by a factor of around 30 parallel to the temperature gradient and by a factor of over 100 perpendicular to the temperature gradient. As Righi–Leduc transport is more dependent on the high velocity part of the distribution function with longer collision times ($q_\wedge \propto \tilde{\propto}\, \omega_c \tau_{ei} q_\perp$), heat flow perpendicular to the temperature gradient is affected more strongly by steep temperature gradients.

At steep temperature gradients, where the heat flow is reduced by non-local effects, further reduction in the heat flow by magnetic confinement only occurs at a higher Hall parameter. Above this threshold Hall parameter, which increases from around $\chi_B = 0.3$ to around $\chi_B = 3$ with increasing $k\lambda$, the local prediction is a fairly good approximation. The high energy electrons responsible for transport are bound more strongly to field lines than the thermal electrons, as $\lambda_{\text{mfp}}/r_c \tilde{e}^{\frac{3}{2}}$, and this first localizes electron transport and then suppresses the transport.

While M1 and hybrid-BGK agree well in the local regime, for the non-local simulations, we see increasing discrepancies. At $k\lambda = 0.012$ and above, hybrid-BGK experiences crashes for Hall parameters above 1, where the heat flow should tend to the local prediction. M1 does give results throughout this domain but gives heat flows below the local prediction by up to a factor of four, disagreeing with the VFP code K2. Both codes are more susceptible to errors in the Righi–Leduc heat flow at high non-localities, due to the strong dependence on high energy groups. Strong magnetisations make M1 more stable but incorrect but make hybrid-BGK more likely to crash.

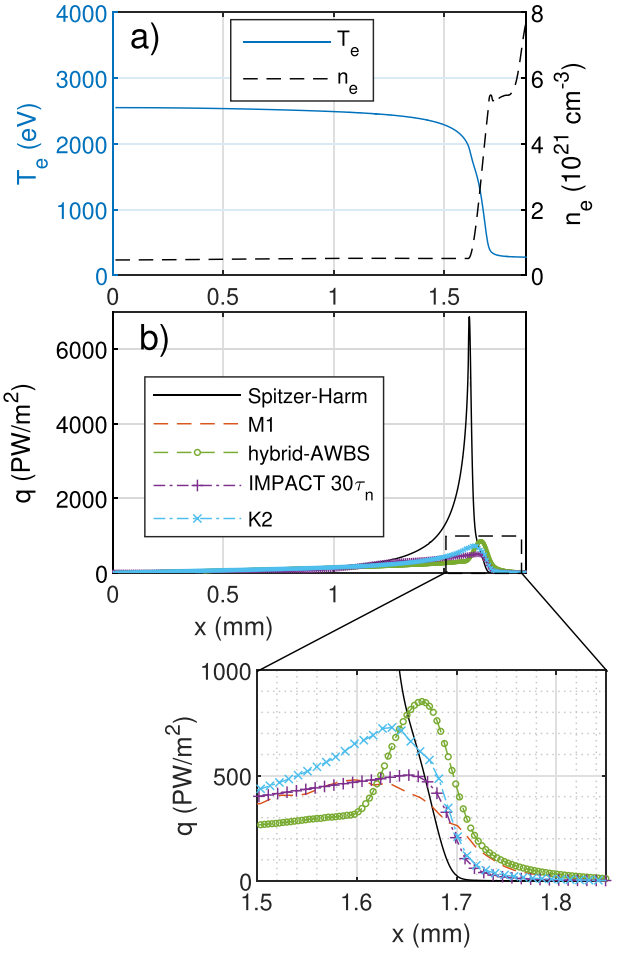

FIG. 11. (a) *Hohlraum* conditions from a one-dimensional HYDRA simulation, showing the electron temperature (solid blue, left axis) and density (dashed black, right axis) from the hot center of the hohlraum to the cold dense material by the wall. The ionization level also varies in space, from $\bar{Z} = 2$ in the helium fill in the center, to $\bar{Z} = 36$ near the wall. (b) The resulting heat flows predicted by Spitzer–Härm (solid black), compared to the predictions from M1 (dashed orange), hybrid-AWBS (dashed green circles), an IMPACT simulations at $30\tau_n$ (dot-dash purple crosses), and a quasi-static K2 simulation (dot-dash blue x's).

V. ICF TEST CASES

A. Hohlraum conditions

We also tested the M1 model in a more realistic situation, using one-dimensional HYDRA simulations of a helium-filled gadolinium hohlraum. An instantaneous snapshot was taken of the spatial profiles for the density, temperature, and ionization level (shown in the top panel of Fig. 11), and this was used to estimate the instantaneous heat flow. The steep temperature gradients near the wall result in a strongly nonlocal situation while the steep density gradient adds an additional challenge to modeling these conditions. A strong cap on the electric field was required to handle these conditions in M1, reducing the field

at the highest electron energies by two orders of magnitude. Even with this, the runtime required by M1 was 9 h, without reaching convergence to zero current.

The resulting heat flow predicted by the Spitzer–Härm model shows an unphysically high heat flow being carried into the hohlraum wall, with over 10^{18} Wm^{-2}. All of the multi-group simulations predict that this heat flow is greatly suppressed, by an order of magnitude at the peak, with the peak in the heat flow shifted around 0.1 mm downstream due to pre-heat.

The multi-group models lie within a factor of two of one another but disagree about the exact degree of pre-heat. Both M1 and hybrid-AWBS estimate a precursor in the heat flow profile around 20 μm further forward compared to the VFP simulations, which both give a precursor 20 μm in advance of the Spitzer–Harm prediction. Over most of the heat flow IMPACT gives a closer match to M1 (within 10%), while hybrid-AWBS predicts a significantly lower heat flow for most of the domain. On the other hand, K2 predicts a peak heat flow amplitude closer to hybrid-AWBS (within 20%).

Note, however, that in the IMPACT simulation the temperature profile also relaxes rapidly over time due to the strong heat flow, meaning that IMPACT predicts a slightly lower heat flow. For this reason, the K2 simulation was run in a quasi-static situation with $\partial_t f_e = \partial_t T_e = 0$ for a more direct comparison with the M1 or hybrid-AWBS simulations, which both assume a quasi-static equilibrium. This means that M1 is probably slightly underestimating the heat flow under these conditions, while hybrid-AWBS is slightly overestimating the heat flow. In this set up K2 also took just 4 s to converge, much faster than all the other codes.

B. 2D "Bubble" tests

Finally, we tested the M1 model in a 2D scenario in order to demonstrate how reducing the collisionality can cause heat flows to be no longer parallel to the local temperature gradient. This is particularly important near the hohlraum wall, where small bubbles form due to laser ablation, with local B fields driven by the Biermann battery term. These reduce the heat flow to the wall. The same simulation parameters were used as for 1D ramp tests, with a plasma density of $n_e = 10^{19}$ cm^{-3} and $Z = 100$, giving $k\lambda_{\text{th}} \approx 3.6 \times 10^{-3}$. The temperature profile was described by a combination of a linear ramp with a colder "bubble" in the center, as

$$T_e[eV] = 300 - 3\tanh(2\pi x[\text{mm}]) - 6\exp\left[-\pi(r[\text{mm}])^2\right]. \quad (41)$$

The M1 model was run on a 101 × 101 grid spanning [−1 mm, 1 mm], using 10 000 energy groups. This calculation took around 10 h on a single core to reach convergence to the current condition. In contrast, the Spitzer–Härm heat flow was calculated in a fraction of a second and a hybrid-BGK simulation took 20 min. A VFP simulation was also performed using IMPACT, taking 48 h on four cores to reach convergence. The M1 model is, therefore, an order of magnitude faster than the kinetic simulation under these moderately nonlocal conditions, but is still too slow to be used on every time step of a fluid code.

The results are shown in Fig. 12. The strong heat flow down the linear ramp is disrupted by the bubble, with q_y components moving heat toward the axis. However, the q_y components are smaller than might be expected such that heat flow predicted by the M1 model is not everywhere parallel to the temperature gradient. This is particularly evident near $x = 0.2$ mm, where heat flow is in some places almost perpendicular to the temperature gradient.

Comparing the heat flows predicted by the different models in Fig. 12(b), we can see that both M1 and IMPACT predict significant flux suppression near the steepest temperature gradient, with the magnitude of the heat flow around half that predicted by Spitzer–Härm. hybrid-BGK predicts even greater flux suppression than M1 and IMPACT, down to around 30%. Near $x = 0.2$ mm the direction of the heat flow is also significantly different, with M1 agreeing closely to the results from IMPACT. We are, therefore, confident that both the M1 model and hybrid-BGK can reproduce nonlocal features in a two-dimensional situation while requiring a fraction of the runtime of a full VFP simulation.

We go further by applying a uniform magnetic field of 25.3 T, chosen such that the Hall parameter at $v_n = \sqrt{2eT_e/m_e}$ is equal to $\omega_c\tau_{ei} = 1$. Again, an M1 simulation took 10 h on a single core, while an IMPACT simulation required 5 h on ten cores to reach convergence. The faster runtime of the magnetized IMPACT simulation is due to the faster convergence in this situation, where the heat flow is both suppressed and localized compared with the unmagnetized case.

The results are shown in Fig. 13. The strong magnetic field causes a large Righi–Leduc component to the heat flow, with the direction of heat flow rotated by almost 90°. The heat flow circulates around the bubble, spiraling down to the minimum in temperature. The heat flow

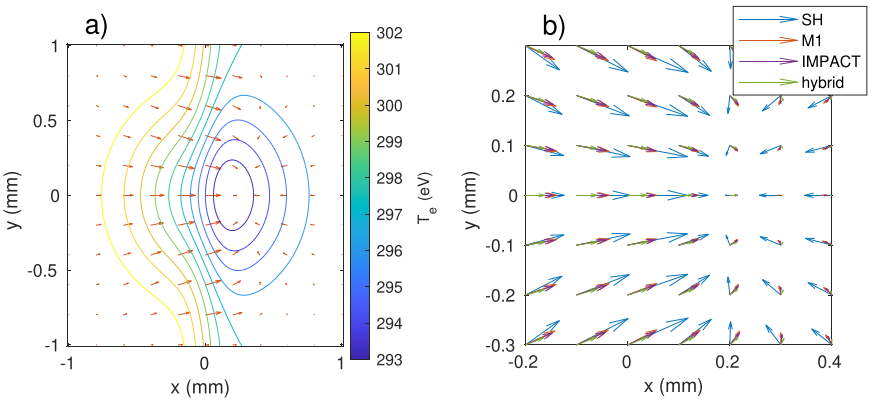

FIG. 12. (a) Temperature profile shown by contours at 1 eV intervals, overlaid with the heat flow predicted by the M1 model, with normalized magnitude described by the length of the arrow. (b) Comparison of the heat flows predicted by the Spitzer–Härm model, M1, hybrid-BGK, and the VFP code IMPACT, all using the same normalization for the arrow length.

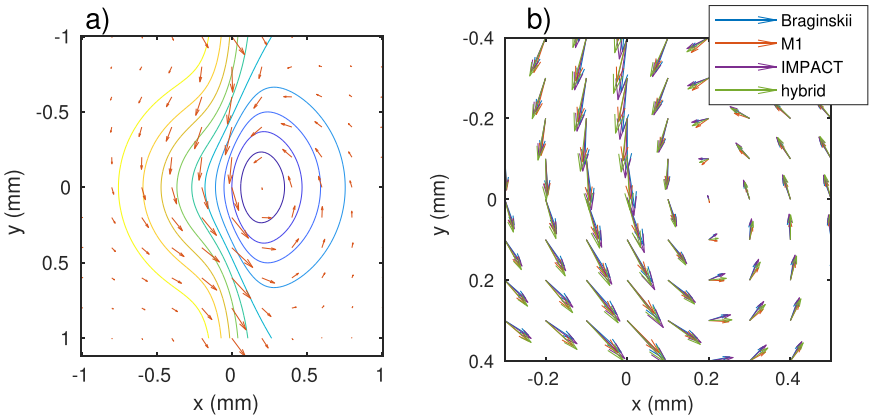

FIG. 13. (a) The temperature profile shown by contours at 1 eV intervals, overlaid with the strongly magnetized heat flow predicted by the M1 model, with normalized magnitude described by the length of the arrow. (b) Comparison of the heat flows predicted by the Braginskii model, M1, hybrid-BGK, and the VFP code IMPACT, all using a normalization for the arrow length ten times lower than in the previous plots.

is also greatly suppressed by the magnetic field, with the peak heat flow around 10 times lower than in the unmagnetized case.

The suppression of the heat flow comes with localization of the heat flow, with all of M1, hybrid-BGK, and IMPACT giving predictions much closer to the local Braginskii predictions for the heat flow. There is very little divergence from the local predictions. On the other hand, there are slight discrepancies between the predictions from M1 and from IMPACT, especially around $x = 0.2$ mm. In this regime, the predictions from the hybrid code are slightly closer to the kinetic simulations. We attribute this to M1 failing to reach convergence to the zero-current condition, even after 25 iterations and 10 h.

C. Electron inertia and time history

It is important to note that in any realistic ICF simulation the evolution of the plasma over time is critical. Currently, both the VFP codes and the reduced multi-group models are starting from an initial condition that can be far from the final converged quasi-static solution. Both K2 and IMPACT in these simulations have started from a Maxwellian form for the electron distribution function, with $f_0 = f_0^m$ as described in Eq. (6) and $\underline{f_1} = \underline{0}$. Both M1 and hybrid-AWBS-BGK, on the other hand, start close to the local Spitzer solution for the distribution function, with $\lim_{v\to\infty} f_0(v) = 0$ and an initial guess for the electric field of $\underline{E_0} = -\frac{5}{2}\underline{\nabla} T_e$. Whereas the Spitzer solution is a good estimate in local and non-magnetized situations, in non-local or strongly magnetized regimes, both approaches are very poor initial estimates, causing slow convergence.

However, the VFP codes include a time history of the plasma dynamics in two ways: explicitly through the electron inertia term $\partial_t f_e$ (which is neglected in the reduced multi-group models) and through calculating the distribution at any time step as a change from the previous time step (often a relatively small change). This second way means that while reaching a converged solution to the quasi-static situations modeled in this paper is initially slow, the simulation remains converged during the subsequent plasma evolution. For instance, for the hohlraum simulation IMPACT required $30\tau_n$ to reach a quasi-steady estimate for the heat flow, taking an hour of runtime, but modeling any subsequent evolution takes just 12 s per $0.1\tau_n$ time step rather than recalculating from initial conditions. This approach could also be included in the reduced models by using the electric field from the previous time step as the initial guess for the next time step, which would greatly speed up convergence.

On the other hand, the reduced models can never capture the effect of electron inertia. As the temperature of the plasma changes as $\partial_t\left(\frac{3}{2} n_e e T_e\right) = -\underline{\nabla} \cdot \underline{q}$, we can estimate the scale of the inertial term in f_0 as

$$\begin{aligned} \partial_t \int v^4 f_e \, \mathrm{d}v &\sim k \int v^5 f_e \, \mathrm{d}v \\ \partial_t f_0 &\sim k v_{\mathrm{th}} f_1. \end{aligned} \tag{42}$$

Assuming that the total distribution function is changing on the same timescale as f_0 and that the collision term is on the scale of $(\partial_t f_e)_{\mathrm{coll}} \sim f_e/\tau$, we can estimate the scale of the total inertial term

$$\begin{aligned} \frac{\partial_t f_e}{f_e} &\sim \frac{\partial_t f_0}{f_0} \sim k v_{\mathrm{th}} \frac{f_1}{f_0} \\ \frac{\partial_t f_e}{(\partial_t f_e)_{\mathrm{coll}}} &\sim k \lambda_{\mathrm{th}} \frac{f_1}{f_0}. \end{aligned} \tag{43}$$

That is, the inertial term can no longer be neglected compared to collisions precisely when transport is strongest and the situation is most non-local. This could well be the case in hohlraum wall simulations like Sec. V A, where by the time the distribution function reaches a steady state in the pre-heat region, the temperature profile near the peak heat flow could have changed. In increasingly non-local situations, the plasma changes on timescales close to the collision time, and there is no longer a quasi-static solution for the distribution function, and reduced multi-group models like M1 and hybrid-AWBS-BGK become progressively less accurate and will ultimately fail to converge to the correct distribution function.

VI. CONCLUSIONS

We have explored using the multi-group M1 and hybrid-AWBS-BGK models to study heat flow in plasmas both with and without a magnetic field. We showed that using an AWBS collision operator together with the quasi-static assumption allows us to estimate the distribution function by solving coupled equations for the zeroth and first moments. Both models perform an explicit integration of the moments of the distribution function in energy and use these to estimate the heat flow while meeting Ampère's law. Whereas M1 assumes a maximal entropy closure and uses an AWBS collision operator for

both moments, hybrid-AWBS-BGK uses an isotropic closure and a BGK collision operator for f_1.

By comparing the predictions from the M1 and hybrid-AWBS-BGK codes to the local models and to the Vlasov–Fokker–Planck code IMPACT, we have shown that both codes successfully reproduce the heat flows in both un-magnetized and magnetized plasmas in the local regime ($K_n < 10^{-6}$, $k\lambda_{\text{th}} < 10^{-4}$) with fast runtimes, particularly for M1. We have shown that M1 also reproduces the correct form for the distribution function, therefore providing a good estimate of other transport properties, such as the electrical conductance.

By looking at linear ramp and cosine problems, we have shown that nonlocality changes the distribution function and leads to the emergence of pre-heat and a reduction in the peak heat flux at $k\lambda_{\text{th}} > 10^{-4}$, which was observed in all of models. We have shown that hybrid-AWBS-BGK tends to be more robust to large non-localities but does fail at $k\lambda_{\text{th}} > 1$. The M1 model matches IMPACT and Epperlein–Short predictions well but crashes earlier, at $k\lambda_{\text{th}} > 0.03$. Introducing a cap to the electric field allows M1 to run on a realistic hohlraum problem with a high Knudsen number. The error in the heat flow is small, on the scale of 10%, but the runtimes for M1 become prohibitively long (> 10 CPU hours) due to the large number of energy groups required (10^6), while hybrid-AWBS-BGK takes less than 1 CPU hour but is less good at capturing the heat flow profile at early times.

Furthermore, we have shown that magnetization makes transport more local, with the peak heat flow tending toward the local prediction when the Hall parameter exceeds $\chi_B > 0.1$. In this regime, hybrid-AWBS-BGK can crash for high non-localities, whereas M1 runs to completion but underestimates the heat flow. An unmagnetized 2D bubble test shows strong divergences from Spitzer–Härm heat flow in both amplitude and direction, but applying a magnetic field brings M1, hybrid-AWBS-BGK, and VFP predictions into close agreement with the local Braginskii model.

ACKNOWLEDGMENTS

This work was performed under the auspices of the U.S. Department of Energy under Contract No. DE-AC52-07NA27344, review no. LLNL-JRNL-873078. The Viking cluster was used during this project, which is a high performance compute facility provided by the University of York. We are grateful for computational support from the University of York, IT Services, and the Research IT team. Thank you to Mehul Patel and Joe Koning for useful discussions. The M1 code was written by CA based on Ref. 27, the hybrid-AWBS-BGK code was written by M.H., and the K2 code was written by M.S.

AUTHOR DECLARATIONS

Conflict of Interest

The authors have no conflicts to disclose.

Author Contributions

C. Arran: Data curation (equal); Investigation (equal); Methodology (equal); Software (equal); Visualization (lead); Writing – original draft (lead); Writing – review & editing (equal). **M. Holec:** Investigation (equal); Methodology (equal); Software (equal); Validation (equal). **M. Sherlock:** Investigation (equal); Methodology (equal); Software (equal); Validation (equal); Writing – review & editing (equal). **M. Marinak:** Conceptualization (lead); Funding acquisition (lead); Methodology (equal); Project administration (lead); Supervision (equal); Writing – review & editing (equal). **C. P. Ridgers:** Conceptualization (equal); Funding acquisition (equal); Methodology (equal); Project administration (equal); Writing – review & editing (equal).

DATA AVAILABILITY

The data that support the findings of this study are available from the corresponding author upon reasonable request.

REFERENCES

[1]A. R. Bell, "Non-spitzer heat flow in a steadily ablating laser-produced plasma," Phys. Fluids **28**, 2007–2014 (1985).
[2]G. Gregori, S. H. Glenzer, J. Knight, C. Niemann, D. Price, D. H. Froula, M. J. Edwards, R. P. J. Town, A. Brantov, W. Rozmus, and V. Y. Bychenkov, "Effect of nonlocal transport on heat-wave propagation," Phys. Rev. Lett. **92**, 205006 (2004).
[3]J. Li, R. Yan, B. Zhao, J. Zheng, H. Zhang, and X. Lu, "Mitigation of the ablative Rayleigh–Taylor instability by nonlocal electron heat transport," Matter Radiat. Extremes **7**, 055902 (2022).
[4]Z. Chen, X. Yang, G. Zhang, Y. Ma, R. Yan, H. Xu, Z. Sheng, F. Shao, and J. Zhang, "Role of nonlocal heat transport on the laser ablative Rayleigh-Taylor instability," Nucl. Fusion **64**, 126029 (2024).
[5]Z. H. Chen, X. H. Yang, G. B. Zhang, Y. Y. Ma, H. Xu, S. X. Luan, and J. Zhang, "Effect of non-local transport of hot electrons on the laser-target ablation," Phys. Plasmas **30**, 062710 (2023).
[6]H. G. Rinderknecht, P. A. Amendt, S. C. Wilks, and G. Collins, "Kinetic physics in ICF: Present understanding and future directions," Plasma Phys. Controlled Fusion **60**, 064001 (2018).
[7]B. E. Peigney, O. Larroche, and V. Tikhonchuk, "Ion kinetic effects on the ignition and burn of inertial confinement fusion targets: A multi-scale approach," Phys. Plasmas **21**, 122709 (2014).
[8]S. T. O'Neill, B. D. Appelbe, A. J. Crilly, C. A. Walsh, D. J. Strozzi, J. D. Moody, and J. P. Chittenden, "Burn propagation in magnetized high-yield inertial fusion," Phys. Plasmas **32**, 022703 (2025).
[9]S. I. Braginskii, "Transport processes in a plasma," Rev. Plasma Phys. **1**, 205 (1965).
[10]E. M. Epperlein and M. G. Haines, "Plasma transport coefficients in a magnetic field by direct numerical solution of the Fokker–Planck equation," Phys. Fluids **29**, 1029–1041 (1986).
[11]D. Froula, J. Ross, B. Pollock, P. Davis, A. James, L. Divol, M. Edwards, A. Offenberger, D. Price, R. Town, G. Tynan, and S. Glenzer, "Quenching of the nonlocal electron heat transport by large external magnetic fields in a laser-produced plasma measured with imaging Thomson scattering," Phys. Rev. Lett. **98**, 135001 (2007).
[12]C. Arran, P. Bradford, A. Dearling, G. S. Hicks, S. Al-Atabi, L. Antonelli, O. C. Ettlinger, M. Khan, M. P. Read, K. Glize, M. Notley, C. A. Walsh, R. J. Kingham, Z. Najmudin, C. P. Ridgers, and N. C. Woolsey, "Measurement of magnetic cavitation driven by heat flow in a plasma," Phys. Rev. Lett. **131**, 015101 (2023).
[13]W. A. Farmer, J. M. Koning, D. J. Strozzi, D. E. Hinkel, L. F. Berzak Hopkins, O. S. Jones, and M. D. Rosen, "Simulation of self-generated magnetic fields in an inertial fusion hohlraum environment," Phys. Plasmas **24**, 052703 (2017).
[14]C. A. Walsh, J. P. Chittenden, K. McGlinchey, N. P. L. Niasse, and B. D. Appelbe, "Self-generated magnetic fields in the stagnation phase of indirect-drive implosions on the National Ignition Facility," Phys. Rev. Lett. **118**, 155001 (2017).
[15]J. D. Sadler, C. A. Walsh, Y. Zhou, and H. Li, "Role of self-generated magnetic fields in the inertial fusion ignition threshold," Phys. Plasmas **29**, 072701 (2022).
[16]P. Y. Chang, G. Fiksel, M. Hohenberger, J. P. Knauer, R. Betti, F. J. Marshall, D. D. Meyerhofer, F. H. Séguin, and R. D. Petrasso, "Fusion yield enhancement in magnetized laser-driven implosions," Phys. Rev. Lett. **107**, 035006 (2011).
[17]M. Hohenberger, P.-Y. Chang, G. Fiksel, J. P. Knauer, R. Betti, F. J. Marshall, D. D. Meyerhofer, F. H. Séguin, and R. D. Petrasso, "Inertial confinement fusion

implosions with imposed magnetic field compression using the OMEGA Laser," Phys. Plasmas **19**, 056306 (2012).
[18]D. S. Montgomery, B. J. Albright, D. H. Barnak, P. Y. Chang, J. R. Davies, G. Fiksel, D. H. Froula, J. L. Kline, M. J. MacDonald, A. B. Sefkow, L. Yin, and R. Betti, "Use of external magnetic fields in hohlraum plasmas to improve laser-coupling," Phys. Plasmas **22**, 010703 (2015).
[19]J. D. Moody, B. B. Pollock, H. Sio, D. J. Strozzi, D. D.-M. Ho, C. A. Walsh, G. E. Kemp, B. Lahmann, S. O. Kucheyev, B. Kozioziemski, E. G. Carroll, J. Kroll, D. K. Yanagisawa, J. Angus, B. Bachmann, S. D. Bhandarkar, J. D. Bude, L. Divol, B. Ferguson, J. Fry, L. Hagler, E. Hartouni, M. C. Herrmann, W. Hsing, D. M. Holunga, N. Izumi, J. Javedani, A. Johnson, S. Khan, D. Kalantar, T. Kohut, B. G. Logan, N. Masters, A. Nikroo, N. Orsi, K. Piston, C. Provencher, A. Rowe, J. Sater, K. Skulina, W. A. Stygar, V. Tang, S. E. Winters, G. Zimmerman, P. Adrian, J. P. Chittenden, B. Appelbe, A. Boxall, A. Crilly, S. O'Neill, J. Davies, J. Peebles, and S. Fujioka, "Increased ion temperature and neutron yield observed in magnetized indirectly driven D2-filled capsule implosions on the National Ignition Facility," Phys. Rev. Lett. **129**, 195002 (2022).
[20]S. A. Slutz and R. A. Vesey, "High-gain magnetized inertial fusion," Phys. Rev. Lett. **108**, 025003 (2012).
[21]M. R. Gomez, S. A. Slutz, A. B. Sefkow, D. B. Sinars, K. D. Hahn, S. B. Hansen, E. C. Harding, P. F. Knapp, P. F. Schmit, C. A. Jennings, T. J. Awe, M. Geissel, D. C. Rovang, G. A. Chandler, G. W. Cooper, M. E. Cuneo, A. J. Harvey-Thompson, M. C. Herrmann, M. H. Hess, O. Johns, D. C. Lamppa, M. R. Martin, R. D. McBride, K. J. Peterson, J. L. Porter, G. K. Robertson, G. A. Rochau, C. L. Ruiz, M. E. Savage, I. C. Smith, W. A. Stygar, and R. A. Vesey, "Experimental demonstration of fusion-relevant conditions in magnetized liner inertial fusion," Phys. Rev. Lett. **113**, 155003 (2014).
[22]R. J. Kingham and A. R. Bell, "An implicit Vlasov–Fokker–Planck code to model non-local electron transport in 2-D with magnetic fields," J. Comput. Phys. **194**, 1–34 (2004).
[23]M. Sherlock, J. P. Brodrick, and C. P. Ridgers, "A comparison of non-local electron transport models for laser-plasmas relevant to inertial confinement fusion," Phys. Plasmas **24**, 082706 (2017).
[24]G. P. Schurtz, P. D. Nicolaï, and M. Busquet, "A nonlocal electron conduction model for multidimensional radiation hydrodynamics codes," Phys. Plasmas **7**, 4238–4249 (2000).
[25]K. H. Ma, M. V. Patel, M. Sherlock, W. A. Farmer, and E. Johnsen, "Thermal transport modeling of laser-irradiated spheres," Phys. Plasmas **29**, 112307 (2022).
[26]B. Dubroca and J.-L. Feugeas, "Etude théorique et numérique d'une hiérarchie de modèles aux moments pour le transfert radiatif," C. R. l'Acad. Sci., Ser. I Math. **329**, 915–920 (1999).
[27]D. D. Sorbo, "An entropic approach to magnetized nonlocal transport and other kinetic phenomena in high-energy-density plasmas," Ph.D. thesis (Universite de Bordeaux, 2016); available at https://theses.hal.science/tel-01280856v1.
[28]M. Holec, J. Nikl, and S. Weber, "Nonlocal transport hydrodynamic model for laser heated plasmas," Phys. Plasmas **25**, 032704 (2018).
[29]J. R. Albritton, E. A. Williams, I. B. Bernstein, and K. P. Swartz, "Nonlocal electron heat transport by not quite Maxwell-Boltzmann distributions," Phys. Rev. Lett. **57**, 1887–1890 (1986).
[30]L. Spitzer and R. Härm, "Transport phenomena in a completely ionized gas," Phys. Rev. **89**, 977–981 (1953).
[31]R. Anderson, J. Andrej, A. Barker, J. Bramwell, J.-S. Camier, J. Cerveny, V. Dobrev, Y. Dudouit, A. Fisher, T. Kolev, W. Pazner, M. Stowell, V. Tomov, I. Akkerman, J. Dahm, D. Medina, and S. Zampini, "MFEM: A modular finite element methods library," Comput. Math. Appl. **81**, 42–74 (2021).
[32]J. D. Huba, *NRL Plasma Formulary* (Naval Research Laboratory, 2013); available at https://library.psfc.mit.edu/catalog/online_pubs/NRL_FORMULARY_13.pdf.
[33]E. M. Epperlein and R. W. Short, "Nonlocal heat transport effects on the filamentation of light in plasmas," Phys. Fluids B **4**, 2211–2216 (1992).